

Supplementary Information

1. VOODOO CAT STATE

In the main article we display the measured and calculated Wigner functions for the resonator states $|0\rangle + |N\rangle$ and for the states $|1\rangle + \exp(ik\pi/8)|3\rangle + |6\rangle$, $k = 0$ to 4. In Fig. S1 we display the “Voodoo cat” state, which involves Fock states as high as $|9\rangle$, fully demonstrating the range of states we can currently prepare.

2. WIGNER TOMOGRAPHY AND DENSITY MATRIX

The Wigner function $W(\alpha)$ and density matrix ρ are related via the trace

$$W(\alpha) = \frac{2}{\pi} \text{Tr} (D(-\alpha)\rho D(\alpha)\Pi). \quad (4)$$

To measure the Wigner function, we first prepare the resonator state, as given by the density matrix ρ . During state analysis, microwaves drive the resonator and coherently displace the resonator state by $-\alpha = (1/2) \int \Omega_r(t)dt$, as described by the operator $D(-\alpha) = D^\dagger(\alpha) = \exp(\alpha^*a - \alpha a^\dagger)$. For the displaced resonator state $\rho' = D(-\alpha)\rho D(\alpha)$, we determine the diagonal elements ρ'_{nn} by measuring $P_e(\tau)$ during a swap interaction⁸ (see below). As the Fock states are eigenstates of the parity operator Π with eigenvalues 1 (-1) for even (odd) Fock states, the Wigner function can simply be calculated as

$$W(\alpha) = (2/\pi) \sum_n (-1)^n \rho'_{nn}(-\alpha). \quad (5)$$

We note that the Wigner function can also be calculated directly from the time trace $P_e(\tau)$ via a Fresnel transform³⁰, requiring only a short time scan, but yielding slightly less precise results in our case. The parity can also be measured directly in the dispersive limit²⁴, obviating the time scan, but the dispersive regime is incompatible with the parameters we need for state preparation.

The amplitude scale and the phase of the microwave pulse α are calibrated by a best fit between the measured and calculated Wigner distributions. Small variations ($\sim 5\%$) in the scale calibration were found for the various states measured here, including the coherent state, and thus an average was used. The magnitude of the scale factor is in good agreement with the attenuation of the microwave line and its coupling capacitor.

The density matrix can be calculated from the Wigner function by inverting Eq. (4). However, to make full use of the measured data, we instead calculate the density matrix ρ directly from the full set of measured photon

number probabilities²⁸ by solving the set of linear equations

$$\rho'_{nn}(\alpha_m) = \langle n|D(-\alpha_m)\rho D(\alpha_m)|n\rangle = \sum_{j,i} M_{nmji}\rho_{ji}, \quad (6)$$

one for each extracted photon number n and one for each measured displacement α_m . The matrix

$$M_{nmji} = \langle j|D(\alpha_m)|n\rangle^* \langle i|D(\alpha_m)|n\rangle, \quad (7)$$

is calculated by expanding the displacement operator $D(\alpha) = \exp(\alpha a^\dagger - \alpha^* a)$ in the Fock basis:

$$\langle p|D(\alpha)|q\rangle = e^{-|\alpha|^2/2} \sqrt{p!q!} \sum_{k=0}^{\min\{p,q\}} \frac{\alpha^{(p-k)}(-\alpha^*)^{(q-k)}}{k!(p-k)!(q-k)!}. \quad (8)$$

We solve the largely overdetermined linear system of Eq. (6) by least-squares while restricting ρ to be hermitian. Due to noise, ρ can have small negative eigenvalues. Therefore we diagonalise ρ , set the unphysical negative eigenvalues to zero, and then transform back to the Fock basis. Finally we normalise ρ .

3. PHOTON NUMBER READOUT

At the end of the state preparation sequence for the resonator, the qubit is ideally in its ground state. We verify this by performing state tomography of the qubit¹⁵, yielding a qubit density matrix that is very close to the ground state. Typically, the off-diagonal elements of the density matrix are very small, but the excited state probability is not zero, corresponding to a Bloch vector pointing close to the $|g\rangle$ state: For the state generation shown in Fig. 4, the angle θ between the Bloch vector and $|g\rangle$ is always smaller than 5° . For the states described in Fig. 3, the angles are from left to right 15° , 3° , 13° , 4° , and 9° , due to less precise tune-up of the sequences for some of the states. The length of the Bloch vector is close to 0.8 in Fig. 4 and slightly larger in Fig. 3. This decrease in amplitude could be due to errors in the preparation sequence that leave the qubit and resonator somewhat entangled. However, we attribute the reduction in visibility mostly to decoherence: The preparation sequences for the states in Fig. 4 take approximately 200 ns, a time slightly longer than the Ramsey coherence time $T_2 = 150$ ns of the qubit. This implies that when the qubit is brought into an equal superposition of $|g\rangle$ and $|e\rangle$ and left there for a time of 200 ns (worst case), the length of the Bloch vector would be reduced to 0.25. The qubit decoherence is actually less than this because the state is typically not in an equal

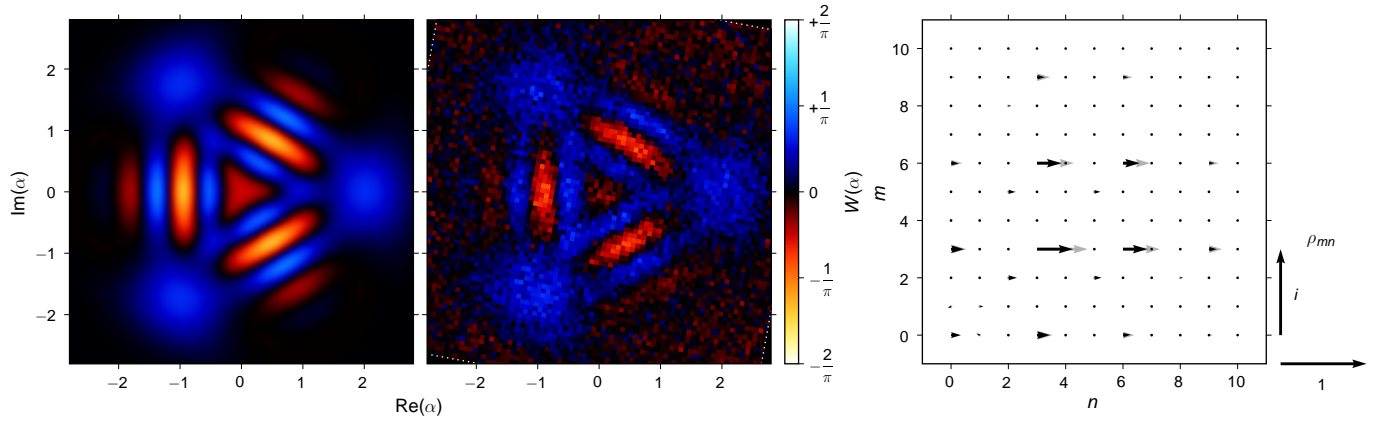


Figure S1 | Wigner tomography of a “Voodoo cat” state. Left panel is theory, middle panel is experiment, and right panel is the comparison of the density matrices, as in the main article. This “Voodoo cat” state is an equal superposition of coherent states $|\alpha = 2\rangle$ (“alive”), $|\alpha = 2e^{2\pi i/3}\rangle$ (“dead”) and $|\alpha = 2e^{4\pi i/3}\rangle$ (“zombie”). The state can be expanded in the Fock basis as $\sum_{n=0,3,6,9,\dots} (2^n/\sqrt{n!})|n\rangle$. For the experimental realisation we have truncated the expansion at $n = 9$. Theory and experiment match well (fidelity $F = 0.83$), indicating that states up to nine photons can be created accurately.

superposition of $|g\rangle$ and $|e\rangle$. In addition, the qubit frequency is partially stabilised when it is interacting with the resonator.

Because the qubit is only weakly entangled with the resonator, we can read out the resonator state with the qubit. In doing so we must account for a reduction in the readout visibility due to the reduced length of the qubit Bloch vector after the preparation sequence.

We perform photon number readout on the resonator

by bringing the qubit on resonance ($\Delta = 0$) for a variable time and then measuring its excited state probability P_e . With the qubit on resonance and no drive signals, all terms in Eq. (1) vanish except for the interaction. If the qubit-resonator state at the beginning of this resonant interaction is described by the system density matrix $\tilde{\rho}$, the probability to measure the qubit in the excited state after time τ is

$$P_e(\tau) = \frac{1}{2} \left(1 - \tilde{\rho}_{(g,0),(g,0)} - \sum_{n=1}^{\infty} ((\tilde{\rho}_{(g,n),(g,n)} - \tilde{\rho}_{(e,n-1),(e,n-1)}) \cos(\sqrt{n}\Omega\tau) + 2\text{Im}(\tilde{\rho}_{(e,n-1),(g,n)}) \sin(\sqrt{n}\Omega\tau)) \right). \quad (9)$$

The qubit is mostly disentangled from the resonator and nearly in the ground state, and thus we can neglect the last two terms of Eq. (9), simplifying this relation to

$$P_e(\tau) \approx \frac{1}{2} \left(1 - P_g \sum_{n=0}^{\infty} P_n \cos(\sqrt{n}\Omega\tau) \right), \quad (10)$$

where P_g is the probability for the qubit to start in its ground state and $P_n = \rho_{nn}$ are the diagonal elements of the resonator density matrix. The probabilities P_n may now be extracted from the measured time evolution $P_e(\tau)$ by performing a least-squares fit of the data with cosine oscillations at the various frequencies $\sqrt{n}\Omega$.

We measure the Rabi coupling frequencies $\sqrt{n}\Omega$ by driving the resonator with a coherent microwave pulse, generating a coherent state, then measuring $P_e(\tau)$. Fourier transforms of $P_e(\tau)$, taken for a range of drive

amplitudes, give sharp peaks at frequencies $\sqrt{n}\Omega$ that are used for calibration.

With P_g and $\sqrt{n}\Omega$ already determined, calculating P_n from Eq. (10) becomes a *linear* least squares fit, which yields stable and robust results.

In our earlier experiment⁸, decay of resonator states during measurement required the introduction of visibility factors. Because coherence times are longer here, visibility factors would be greater than 95% and are not absolutely required to correct for the decay of the Fock states during measurement. Nevertheless, the precision of the photon number analysis was improved by including decoherence into the calculation of $P_e(\tau)$. We numerically solve the Lindblad master equation³¹ for the qubit coupled to Fock states, including the same Hamiltonian evolution as Eq. (1) but with the relaxation times $T_{1,r} = 3.5 \mu\text{s}$ for the resonator and $T_{1,q} = 650 \text{ ns}$ for the

qubit and using the dephasing time $T_{\phi,q} = 300$ ns for the qubit (resonator dephasing is much slower than $3.5 \mu\text{s}$ and not included in the model). Note that we use a larger qubit dephasing time than measured for the qubit alone, which accounts for the stabilising effect of the resonator on the qubit. As we do not know of any theory precisely predicting this stabilising effect, the qubit dephasing parameter was adjusted to best match the observed time evolution.

Although we typically fit for photon numbers up to $n_{\text{fit}} = 15$, the results are significant only up to $n_{\text{max}} = 10$. We fit more photons than needed because the oscillations from P_n are not orthogonal, so P_n from the highest n absorbs some probability from non-fitted photon numbers.

4. PULSE CALIBRATION

As illustrated in Table 1 in the main article, the intermediate states during state generation are quite complex. This complexity discourages the measurement of intermediate states to tune the sequences. Instead, we carefully calibrate the fundamental operations, the single qubit Rabi pulse, the qubit-resonator photon swap, and the qubit-resonator phase accumulation, thus obviating the need to tune up individual sequences. The calibrations of the microwave electronics described here are fully automated. The qubit calibrations are semi-automated and require standard adjustments of the bias and read-out, which are not detailed here.

4.1. Calibration of the microwave circuitry

We control the qubit using flux bias and microwave pulses. The flux bias is applied via two separate signal lines, one heavily low-pass filtered but weakly attenuated allowing large flux bias excursions at low speed, the other unfiltered but heavily attenuated allowing small excursions at high rates. The lines are combined in the experimental cryostat at a custom inductive bias-tee just outside of the sample mount. This summed current inductively couples magnetic flux to the qubit. The microwave line has two broadband (20 GHz) 20 dB attenuators placed at 4 K and the mixing chamber and capacitively couples current to the qubit.

4.1.1. Slow flux bias

The slow flux-bias waveform is generated by a custom low-speed and high-accuracy digital to analog converter (DAC) based on the MAX542³². For low noise performance, its digital inputs and clock are held constant during qubit operation.

4.1.2. Fast flux bias

The fast flux-bias waveform is generated by custom DAC electronics³² based on the AD9736, which gives 14 bit resolution at a 1 GHz sampling rate. Its two differential outputs are sent through separate Gaussian low-pass filters³² with a 3 dB roll-off frequency of 200 MHz, and then to a differential amplifier (THS4509) for low distortion amplification and conversion to a single-ended output. To correct for imperfections in this electronics chain, we first generate a step-edge output from the DAC and measure with a sampling oscilloscope the output waveform. Using de-convolution techniques, we then digitally correct any desired waveform with the measured response of the step-edge.

The 200 MHz low-pass filters considerably suppress signals close to the DAC Nyquist frequency of 500 MHz. The de-convolution correction compensates for this suppression and greatly amplifies signal components close to the Nyquist frequency, causing various artifacts. We add a software low-pass filter to prevent this amplification of high frequency components, as well as ringing due to a sharp cutoff at the Nyquist frequency. We found that a Gaussian low-pass filter with a 3 dB frequency of 150 MHz, worked well with our electronics chain.

This calibration from the sampling oscilloscope eliminates all distortions outside the cryostat. Wiring imperfections inside the cryostat may also be measured and corrected by using the qubit as a sampling oscilloscope. We use the flux-bias dependence of the qubit transition frequency to measure how the actual flux bias evolves in time: We first tune a 8 ns FWHM resonant microwave π -pulse in amplitude and frequency to yield a high fidelity $|g\rangle \rightarrow |e\rangle$ qubit transition (see below). We then add a $1 \mu\text{s}$ flux-bias pulse just before the microwave pulse. The flux waveform is much longer than the ~ 100 ns timescale over which imperfections are observed, so we only consider the second (falling) flank of the waveform. In the absence of imperfections, the flux bias following the test waveform will settle to its pre-waveform value, and the microwave swap pulse will be precisely resonant with the $|g\rangle \rightarrow |e\rangle$ transition. In actuality, we find that the qubit frequency is slightly de-tuned, so the π -pulse fidelity is reduced. We then add a flux bias offset to bring the qubit back on resonance and return the fidelity of the π -pulse to its original value. By scanning flux offset and timing, we can map out the response of the qubit to the flux bias step. We then correct for this response in the same way as for the response function measured with the oscilloscope. Because this method has only a limited time resolution due to the finite length of the microwave pulse, we correct for fast distortions outside the cryostat.

4.1.3. Microwave drive

For the microwave drive for qubit and resonator we use a single microwave source (Anritsu 68369A/NV), modulated by IQ mixers (Marki IQ0307LXP). The I and Q channels of each mixer are driven by two DAC outputs identical to the fast flux bias. The mixers generate single-sideband microwaves that can vary in frequency, phase, and amplitude. We phase-lock all five DAC channels to an external 10 MHz clock, and digital communication between the DACs ensures that the waveforms are synchronised with each other and the microwave source. We perform 3 types of calibrations for the microwave signals:

DAC zero adjustment ensures that the IQ mixer output can be turned off precisely, eliminating bleed-through of the carrier signal. In principle, a small magnitude of carrier leakage is not a problem because, as we use sideband mixing, the carrier frequency is typically not resonant with the qubit or resonator. However, we typically place the carrier frequency between qubit and resonator frequency. Since the qubit is swept through the carrier frequency each time it is tuned into resonance with the resonator, carrier leakage could slightly perturb the qubit state. To calibrate the I and Q DAC values needed to zero out the mixer, we measure the mixer output with a spectrum analyser in a very narrow frequency band around the carrier frequency. A simple search allows both I and Q to be zeroed: We first fix the Q channel DAC and measure the power for 3 different I DAC values, finding the minimum from a parabolic fit. We then fix this I value and measure the power for three Q values, finding the best Q value in the same way. This sequence is repeated over increasingly narrow ranges until the resolution of the DAC is reached. We typically find carrier on/off ratios of > 70 dB. We also find DAC values for zero are strongly dependent on carrier frequency.

Sideband mixing generates a shift $\Delta\omega$ in the carrier frequency ω by applying a signal of frequency $\Delta\omega$ to the I and Q ports of the mixer. A single sideband is generated when the signal to port Q is phase shifted by $\pi/2$ with respect to port I. IQ mixers are imperfect, and deviations exist in both the amplitude sensitivities and the relative phase, which gives rise to an opposite frequency sideband at $-\Delta\omega$. We cancel this undesired signal by adding to the digital I and Q waveforms a compensating signal of adjustable amplitude and phase at $-\Delta\omega$. To adjust this compensating signal, we measure the undesirable sideband signal with a spectrum analyser and adjust the real and imaginary part of the compensation to achieve an absolute minimum, with the same search pattern as for zeroing of the DACs. We find the compensation depends both on the carrier frequency ω and the sideband frequency $\Delta\omega$.

Deconvolution calibration is similar to that performed for the flux bias signal. Here, we measure the pulse response at microwave frequencies. After calibrating the

DAC zero and sideband mixing, we apply a 1 ns impulse to port I and measure the output of the IQ mixer with a sampling oscilloscope. The impulse response is then obtained by numerically demodulating the carrier frequency. The same measurement is then repeated for port Q. As this calibration is slow, it is performed only for a single carrier frequency, typically 6 GHz. This simple calibration is sufficient because the microwave signals do not have stringent requirements on the pulse shape. We find precise calibration of the sideband mixing is of greater importance.

4.2. Qubit microwave pulses

When microwave pulses are used to generate qubit transitions $|g\rangle \leftrightarrow |e\rangle$, excitations to higher energy levels must be avoided, in particular the next higher eigenstate $|2\rangle$. The $|2\rangle \leftrightarrow |e\rangle$ transition frequency is typically 200 MHz lower than $|e\rangle \leftrightarrow |g\rangle$ due to the limited non-linearity of the phase qubit. Microwave pulses for $|g\rangle \leftrightarrow |e\rangle$ therefore need to have low spectral component at the $|e\rangle \leftrightarrow |2\rangle$ transition frequency, so the pulses must be sufficiently long and accurately shaped. We program the pulses to have Gaussian envelopes with 8 ns FWHM, which were measured to yield negligible population ($\lesssim 10^{-4}$) of the $|2\rangle$ state³³.

We calibrate single qubit Rabi pulses with the $|g\rangle \rightarrow |e\rangle$ transition, which corresponds to a rotation π on the Bloch sphere. For this calibration, we maximise the measured probability P_e by adjusting the amplitude and frequency of the microwaves, as described in a previous experiment³³ that obtained a gate fidelity of 98%. For Bloch sphere rotations with smaller angles, we simply scale the pulse amplitude. Nonlinearities in the DAC and from the AC Stark effect generate errors of less than 2% in the rotation angle.

4.3. On-resonance tuning

We typically de-tune the qubit by ≈ 500 MHz below the resonator frequency for a qubit-resonator coupling of $\Omega/2\pi \approx 20$ MHz. By operating below the resonator frequency, the qubit is not swept through this resonance when measured and higher level transitions of the qubit do not cross the resonator frequency. To calibrate the flux bias pulse that tunes the qubit into resonance with the resonator, we prepare the qubit in the $|e\rangle$ state using a microwave Rabi pulse (see above), apply a flux bias tuning pulse with a variable amplitude and duration, and then measure the excited state probability P_e . Close to resonance, a single photon is swapped between the qubit and resonator at the frequency

$$\Omega' = \sqrt{\Omega^2 + \Delta^2} \quad (11)$$

which equals the coupling strength Ω when the qubit and resonator are on resonance ($\Delta = 0$). The resonance condition is precisely measured by varying the tuning pulse amplitude and duration τ , mapping out P_e as shown in Fig. 2 of the article. We then Fourier transform $P_e(\tau)$ for different flux biases, and fit the maxima of the Fourier transform to Eq. (11) to find the flux bias amplitude that gives the minimum swap frequency. This fit is shown in Fig. 2d of the article.

4.4. Swap pulse calibration

With the magnitude of the flux bias pulse determined from the previous calibration step, we next precisely adjust the length of the swap pulse so that the photon is completely transferred from the qubit to the resonator. We optimise transfer by minimising the probability P_e of finding the qubit in its excited state after the transfer.

The shape of the rising and falling edges of the flux bias pulses is defined by the 150 MHz numerical Gaussian low-pass filter (see section 4.4.1), and is error-function shaped with a 10% to 90% rise time of 2.3 ns. The finite duration of the pulse rise and fall time, during which the qubit is approaching resonance while interacting with the resonator, limits the fidelity of the photon transfer. To compensate for this effect, we add a Gaussian-shaped overshoot to the beginning and end of the pulse, bringing the qubit frequency slightly past the resonator frequency. The Gaussian is centred at the step edge and its FWHM of 2.1 ns is also defined by the numerical low-pass filter. The pulse duration and overshoot height are adjusted alternately several times to reach the global minimum in P_e .

Once the transfer of the first photon is optimised, we repeat the procedure for the second photon: A microwave Rabi pulse is added immediately after the first swap pulse bringing the qubit into the $|e\rangle$ state, and then the swap pulse is optimised for minimum P_e . We typically repeat this optimisation procedure for up to six photons, which represents generation of Fock states in the resonator. The amplitude of the optimal overshoot only depends weakly on photon number. As calibration cannot depend on photon number for arbitrary state generation, we average the overshoot and apply this value for all the swap pulses. Using the average overshoot, we then repeat the calibration procedure for only the pulse duration, finding swap times for up to 15 photons.

We use these swap times to calibrate the swap operation for arbitrary state generation. Since the coupling strength scales as \sqrt{n} , where n is the photon number, the n -photon swap time will result in a swap angle of $\phi = \pi/\sqrt{n}$ when applied to the ground state of the resonator. Thus, when plotted versus $1/\sqrt{n}$, as in Fig. S2, all swap times should fall on a line, whose slope and intercept give the calibration for the swap operation.

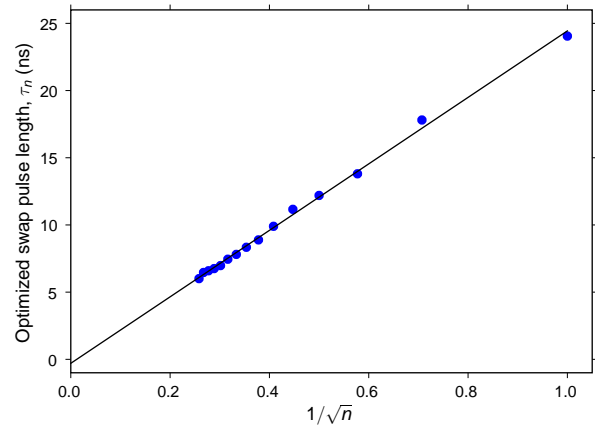


Figure S2 | Calibration of the photon swap operation from the measurement of optimum swap time versus $1/\sqrt{n}$. The optimum time for the n -photon swap pulse is measured by maximising state transfer to the resonator, resulting in the generation of Fock states. Because coupling strength scales as \sqrt{n} , the data should fall on a line. The slope and offset time of this line is used to calibrate the swap operation for arbitrary state generation.

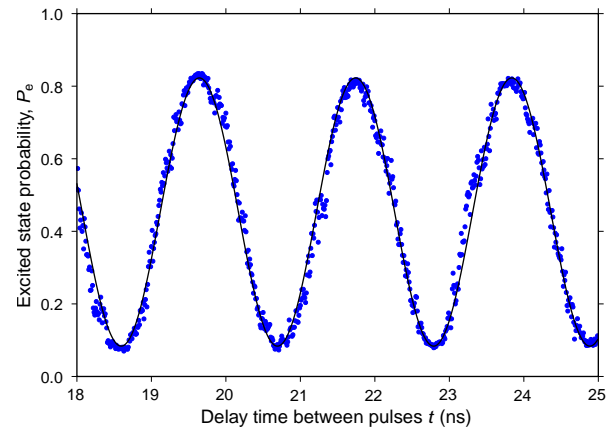


Figure S3 | Ramsey interferometry between qubit and resonator. The sequence consists of a qubit π pulse followed by two half-swaps separated by a variable delay time t , then measurement of the qubit state. Delay times t only need to be scanned around 20 ns, which are relevant for the arbitrary state pulse sequence.

4.5. Phase accumulation rate

When the qubit is de-tuned from the resonator, the $|e, n\rangle$ states accumulate phase with respect to the $|g, n+1\rangle$ states at a rate $\Delta_{\text{off}} = \omega_q - \omega_r$, roughly $-2\pi \times 500$ MHz. For generating states more complex than Fock states, this phase must be taken into account. To calibrate phase accumulation, Ramsey interferometry is used between the qubit and resonator: We first prepare the qubit in the $|e\rangle$ state with a swap pulse, and then perform a half-swap to the resonator. After a variable time t we perform a

second half-swap, and measure P_e as a function of t . As seen in Fig. S3, the probability oscillates sinusoidally at the phase accumulation rate. The two half-swaps add to a full swap, yielding a minimum P_e , when the delay time t yields a phase accumulation of a multiple of 2π . For phase accumulation of π , the second half-swap undoes the first half-swap, yielding a maximum value for P_e . The oscillation allows a precise calibration of phase accumulation when the qubit and resonator are de-tuned.

Note that the timing of the pulses in Fig. S3 require nearly continuous variation of t . The pulse edges can be adjusted for a time much less than the 1 ns DAC update time because the step edges are generated from several DAC points. As illustrated in Fig. S3, we can adjust and control the step edges in the 10 – 50 ps range.

References

8. Hofheinz, M. *et al.* Generation of Fock states in a superconducting quantum circuit. *Nature* **454**, 310–314 (2008).
15. Steffen, M. *et al.* State tomography of capacitively shunted phase qubits with high fidelity. *Phys. Rev. Lett.* **97**, 050502 (2006).
24. Haroche, S. & Raimond, J.-M. *Exploring the Quantum — Atoms, Cavities and Photons* (Oxford, 2006).
28. Leibfried, D. *et al.* Experimental determination of the motional quantum state of a trapped atom. *Phys. Rev. Lett.* **77**, 4281–4285 (1996).
30. Lougovski, P. *et al.* Fresnel representation of the Wigner function: An operational approach. *Phys. Rev. Lett.* **91**, 010401 (2003).
31. Lindblad, G. On the generators of quantum dynamical semigroups. *Comm. Math. Phys.* **48**, 119–130 (1976).
32. For detailed information and schematics see <http://www.physics.ucsb.edu/~martinisgroup/electronics.shtml>.
33. Lucero, E. *et al.* High-fidelity gates in a single Josephson qubit. *Phys. Rev. Lett.* **100**, 247001 (2008).